



AIAA 2002-2746

**Heat Shield Cavity Parametric Experimental
Aeroheating for a Proposed Mars Smart
Lander Aeroshell**

Derek S. Liechty and Brian R. Hollis
NASA Langley Research Center
Hampton, VA

**32nd AIAA Fluid Dynamics Conference and
Exhibit**

**June 24-27, 2002
St. Louis, Missouri**

HEAT SHIELD CAVITY PARAMETRIC EXPERIMENTAL AEROHEATING FOR A PROPOSED MARS SMART LANDER AEROSHELL

Derek S. Liechty^{*}, Brian R. Hollis[†]
NASA Langley Research Center
Hampton, VA

ABSTRACT

The proposed Mars Smart Lander is to be attached through its aeroshell to the main spacecraft bus, thereby producing cavities in the heat shield. To study the effects these cavities will have on the heating levels experienced by the heat shield, an experimental aeroheating investigation was performed at the NASA Langley Research Center in the 20-Inch Mach 6 Air Tunnel. The effects of Reynolds number, angle-of-attack, and cavity size and location on aeroheating levels and distributions were determined and are presented. To aid the discussion on the effects of the cavities, laminar, thin-layer Navier-Stokes flow field solutions were post-processed to calculate relevant boundary layer properties such as boundary layer height and momentum thickness, edge Mach number, and streamwise pressure gradient. It was found that the effect of the cavities varies with angle-of-attack, freestream Reynolds number, and cavity size and location. The presence of a cavity raised the downstream heating rates by as much as 325% as a result of boundary layer transition.

NOMENCLATURE

<p>h heat transfer coefficient, $h=q/(H_{aw}-H_w)$, (slug/ft²/s or kg/m²/s)</p> <p>H enthalpy (BTU/lbm or J/kg)</p> <p>L length of vehicle from nose to base (in. or m)</p> <p>M Mach number</p> <p>p pressure (lb/in² or Pa)</p> <p>q surface heat transfer rate (BTU/ft²/s or W/m²)</p> <p>R model reference radius (in. or m)</p> <p>R_b model base radius (in. or m)</p> <p>R_n model nose radius (in. or m)</p> <p>R_s model shoulder radius (in. or m)</p> <p>Re unit Reynolds number (1/ft or 1/m)</p> <p>r radial distance from symmetry axis (in. or m)</p> <p>s distance along surface from cavity center (in. or m)</p> <p>u velocity magnitude (ft/s or m/s)</p> <p>w cavity diameter (in. or m)</p> <p>α angle-of-attack (deg)</p> <p>δ boundary layer height (in or m)</p>	<p>ϕ model orientation angle (deg)</p> <p>η body half angle (deg)</p> <p>Θ momentum thickness ($\Theta=\int(\rho u/\rho_e u_e)*(1-u/u_e)dy$) (in or m)</p> <p>$\theta$ cavity orientation angle (deg)</p> <p>ρ density (slug/ft³ or kg/m³)</p> <p>ξ first afterbody cone angle (deg)</p> <p>ζ second afterbody cone angle (deg)</p>	<p><u>Subscripts</u></p> <p>∞ freestream static conditions</p> <p>aw adiabatic wall conditions</p> <p>e boundary layer edge conditions</p> <p>FR conditions from Fay-Riddell calculation for a hemisphere</p> <p>fs full scale dimensions</p> <p>w conditions evaluated at the wall</p>
---	---	---

INTRODUCTION

The design¹ of the proposed Mars Smart Lander (MSL) aeroshell requires that it be attached to the main spacecraft bus by way of six structural inserts which pass through holes in the forebody heat shield (Fig 1). When the lander is separated from the spacecraft bus prior to entry into the Martian atmosphere, the bolts are severed and retracted, which forms cavities. The presence of these cavities in the heat shield during entry may result in high, localized heating at the downstream edge of the cavities due to flow separation and reattachment

^{*} Aerospace Technologist

[†] Aerospace Technologist, Senior Member AIAA

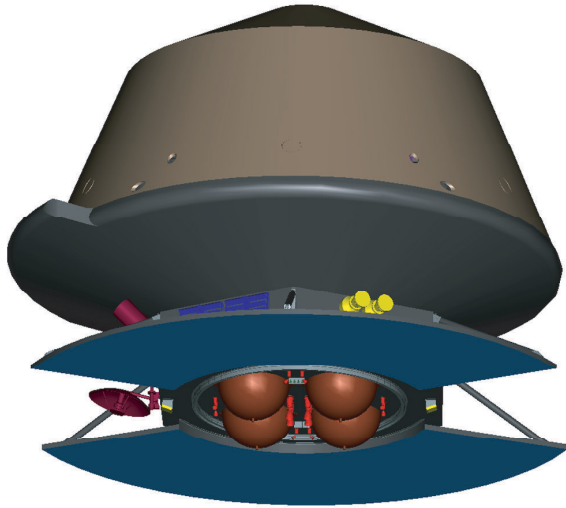


Figure 1: MSL cruise configuration.

within the cavities; and may be accompanied by a heating augmentation downstream of the cavities due to a change in the state of the boundary layer from laminar to transitional or turbulent. The Genesis Sample Return Capsule² (GSRC) also contains forebody heat shield cavities, but there are several significant differences between the two vehicles. First, the forebody half angle of the GSRC is different than the proposed MSL. Also, the proposed MSL is being designed to enter the Martian atmosphere at an angle-of-attack of 16-deg, but most of the data for the GSRC collected in Ref. 2 were at 0-deg angle-of-attack.

The goal of the present study is to determine experimentally how these cavities affect the heating levels on the forebody of a MSL concept. Tests were conducted at nominal conditions of Mach 6 in air with freestream Reynolds numbers from 2.1×10^6 to 7.3×10^6 per foot. A range of angles-of-attack from 0-deg to 20-deg was studied. These conditions result in boundary layer edge conditions similar to those found in flight³. Transition correlations have been developed that relate the Reynolds number based on momentum thickness to the ratio of cavity diameter to boundary layer thickness for the wind tunnel conditions in Ref. 4 and for flight conditions in Ref. 3. Three nominal cavity sizes were tested at two radial locations. Global heating distributions were measured using thermographic phosphors. To complement the measurements made in the wind tunnel, laminar, thin layer Navier-Stokes flow field solutions generated using the Langley Aerothermodynamic Upwind Relaxation Algorithm^{5,6} (LAURA) were post pro-

cessed to calculate boundary layer height, momentum thickness, edge Mach number, and streamwise pressure gradients. Only a qualitative discussion of boundary layer properties will be included in this report. Corresponding computations and correlations for this study are presented in the companion paper by Hollis⁴.

EXPERIMENTAL METHODS

Test Facility

Aeroheating tests were conducted in the NASA Langley 20-Inch Mach 6 Air Tunnel. This is a blow-down facility in which heated, dried and filtered air is used as the test gas. The tunnel has a two-dimensional, contoured nozzle that opens into a 20.5-in. by 20-in. test section. The tunnel is equipped with a bottom-mounted injection system that can transfer a model from the sheltered model box to the tunnel centerline in less than 0.5 seconds. Run times of up to 15 minutes are possible in this facility, although for the current aeroheating test, run times of only a few minutes were required (models are only exposed to the flow for a few seconds). The nominal reservoir conditions of this facility are stagnation pressures of 30 to 500 psia (206.8 to 3447.4 kPa) with stagnation temperatures of 760° to 1000°R (422.2 to 555.5 K), which produce perfect gas freestream flows with Mach numbers between 5.8 and 6.1 and Reynolds numbers of 0.5×10^6 to 7.3×10^6 per foot (1.64×10^6 to 23.95×10^6 per meter). A more detailed description of this facility is presented in Ref. 7.

Phosphor Thermography Technique

Global surface heating distributions were calculated using the digital optical measurement method of two-color, relative-intensity, phosphor thermography⁸⁻¹¹. Ceramic wind tunnel models are coated with a phosphor compound that fluoresces in two separate regions (green and red) of the visible light spectrum. During a wind tunnel run, the phosphor-coated model is illuminated by ultraviolet (UV) light sources, and the resulting fluorescent intensity of the model is recorded and digitized through a color CCD (charge coupled device) camera. The fluorescent intensity is dependent on both the intensity of the incident UV light and the local model surface temperature. The UV intensity dependence is removed by taking the ratio of the green to red intensity images, from which surface temperature distributions can be determined through prior calibrations. Images are acquired before the wind tunnel run and after injection of the model to the tunnel centerline during a run.

Global heat transfer distributions are then computed from these temperature data using one-dimensional, constant heat-transfer coefficient conduction theory¹¹.

The global phosphor thermography technique is now the standard method for aeroheating studies in Langley’s hypersonic tunnels used for aerothermodynamic studies. The global data obtained using this method can be used to identify the surface heating effects of complex three-dimensional flow phenomena such as transition fronts, vortex structures, and shock interactions which are difficult to examine using conventional discrete-sensor methods such as thin-film resistance gages or coaxial surface thermocouples.

Test Model Description

In order to manufacture ceramic test models, rapid-prototype, stereolithographic (SLA) resin models were first fabricated based on surface geometry definitions in electronic data files. Wax molds of the resin models were made, and then a patented¹² silica ceramic slip casting technique was used to form a ceramic shell of the models. The shell was then back-filled with a hydraulically setting magnesia ceramic for strength and support. Finally, the models

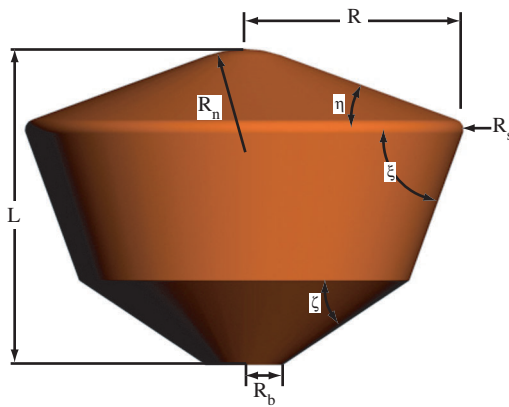


Figure 2: MSL geometry.

Parameter	Full Scale	Test Model
R (in.)	79.72	2.50
R_n (in.)	38.79	1.218
R_s (in.)	3.89	0.122
R_b (in.)	13.95	0.438
L (in.)	114.52	3.596
η (deg)	20	20
ξ (deg)	70	70
ζ (deg)	33.6	33.6

Table 1: Parameters for MSL geometry.

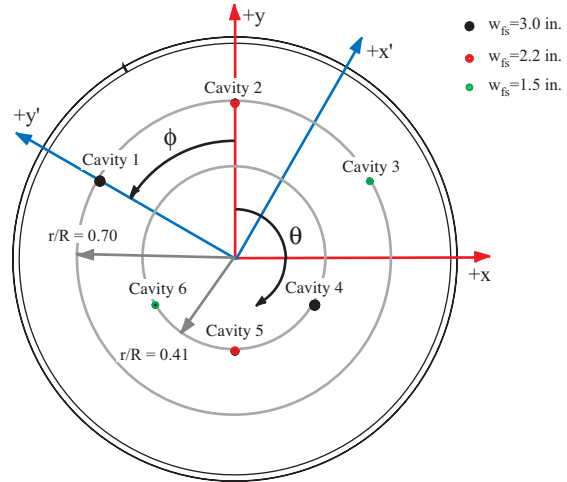


Figure 3: MSL model and cavity orientation.

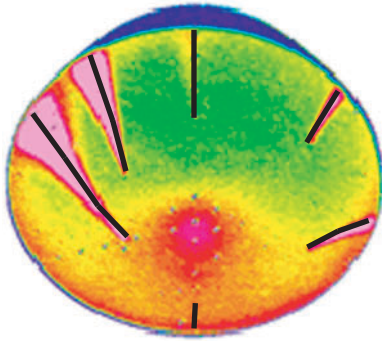
were coated with a mixture of phosphors suspended in a silica-based colloidal binder.

The proposed MSL entry vehicle is a 70-deg sphere-cone with a biconic afterbody. The geometry of the proposed MSL aeroshell is shown in Fig. 2 and its dimensions (full scale and test model) are shown in Table 1. The forebody will have six cavities of the same size and radial location spaced at 60-deg increments, although the final size and locations have not been determined.

The cast ceramic aeroheating models were 5-in. diameter, 0.0314-scale representations of a proposed 13.29-ft diameter Mars Smart Lander aeroshell. Two model configurations were tested in this study. The first was a baseline configuration model without any cavities. The second configuration was a cavity parametric model (Fig. 3). It had a total of six cavities located 60-degrees apart around the forebody. Three cavity diameters ($w_{fs} = 1.5$ -in., 2.2-in., and 3.0-in.) and two radial locations ($r/R = 0.41$ and 0.70) were included in this study. Each of the six cavities has been given a number and the radial locations and diameters of each are presented in Table 2.

Cavity Number	r/R	w_{fs} (in.)
1	0.70	3.0
2	0.70	2.2
3	0.70	1.5
4	0.41	3.0
5	0.41	2.2
6	0.41	1.5

Table 2: Cavity numbering system for the MSL.



(Data extractions shown as black lines.)

Figure 4: Example data extraction lines.

In order to refer to the cavities as model orientation changes, two angles are defined. First, the model orientation angle, ϕ , is defined as 0-deg when cavity 1 is on the vertical upright in an image, and increases as the model is rotated counterclockwise (Fig. 3; cavity 1 is always on the $+y'$ axis). The second angle, θ , is the cavity orientation angle measured clockwise from the vertical upright in an image ($\theta = 0$ -deg on the vertical upright regardless of the value of ϕ).

Small, circular marks were placed on the models to aid in data reduction and model orientation. These marks, referred to as fiducial marks, do not influence the flow over the model surface. The fiducial marks can be seen in run images as dark dots and should not be confused with cavities.

Data Reduction

One-dimensional, semi-infinite solid heat conduction theory¹¹ was used to compute surface heating distributions from the global surface temperature data acquired through phosphor thermography. A constant heat-transfer coefficient is assumed in this theory, and empirical corrections¹¹ are made to account for changes in model substrate thermal properties with temperature. Phosphor images were acquired shortly after injection of the model to the tunnel centerline, which requires less than one second.

Data cuts were extracted from the heat transfer images. Example data extraction locations are given in Fig. 4. Results are presented herein in terms of a non-dimensional heat transfer coefficient ratio, h/h_{FR} , where h_{FR} is the theoretical heating computed with the Fay-Riddell¹³ method for a 1.2165-in. (3.09 cm) sphere, which is the radius of the spherical portion of the forebody of the test models, at 300 K.

As detailed in Ref. 11, the estimated uncertainty of the phosphor thermography technique is approximately $\pm 13\%$ on the forebody.

Test Matrix and Tunnel Conditions

The data were collected on the baseline smooth model at angles-of-attack of 0-deg, 11-deg, 16-deg and 20-deg and freestream Reynolds numbers between 2.1×10^6 and 5.8×10^6 per foot. The cavity parametric models were tested at angles-of-attack of 0-deg, 11-deg, 16-deg and 20-deg at freestream Reynolds numbers between 2.4×10^6 and 7.3×10^6 per foot. The nominal test conditions are presented in Table 3.

RESULTS AND DISCUSSION

Flow Field Computations

MSL flow field computations⁴ were performed using the Langley Aerothermodynamic Upwind Relaxation Algorithm^{5,6} (LAURA) at test facility conditions for laminar flow. A comparison between measured experimental heating and computational heating predictions can be seen in Fig. 5. (A detailed discussion of boundary layer transition correlation and an aeroheating prediction analysis of the MSL for wind tunnel conditions is presented in the companion paper by Hollis⁴.)

In order to determine MSL boundary layer properties, an algorithm to was written to post-process the LAURA output files to extract boundary layer edge

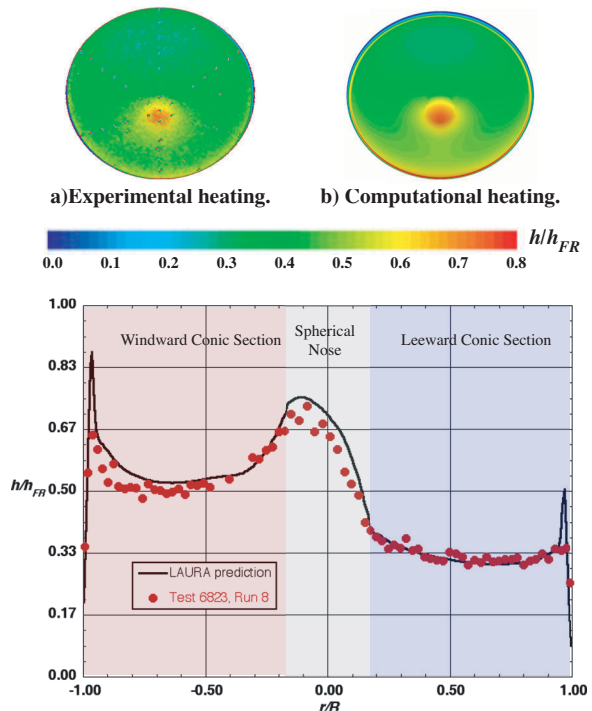


Figure 5: Comparison of experimental and computational results at $Re_\infty = 3.0 \times 10^6/\text{ft}$, $\alpha = 16$ -deg.

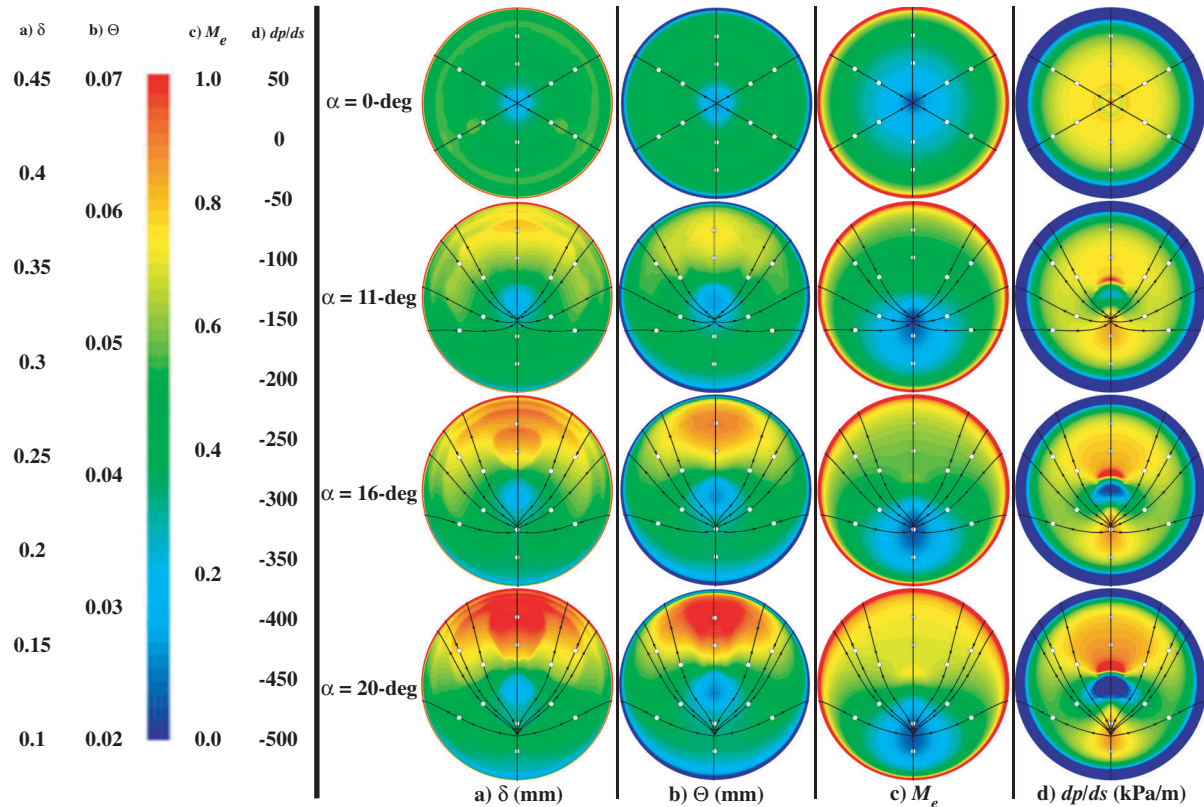


Figure 6: Effect of angle-of-attack on boundary layer properties at $Re_\infty = 3.0 \times 10^6/\text{ft}$.

conditions. The boundary layer height (δ) was defined as the distance along the wall surface normal at which the stagnation enthalpy is equal to 99.5% of the freestream value. Flow properties were interpolated at discrete points along the wall surface normal and a numerical integration was performed to calculate the boundary layer momentum thickness (Θ). The streamwise pressure gradient and Mach number were also calculated at the boundary layer edge. In the images presented in this section, all possible cavity locations are shown as white circles and streamlines are shown through all cavity locations.

The effects of angle-of-attack are shown in Figure 6 at $Re_\infty = 3.0 \times 10^6/\text{ft}$. As angle-of-attack was increased, δ and Θ on the windward surface of the forebody decreased, while on the leeward surface, they increased as expected. M_e increased on the leeward surface of the forebody as angle-of-attack was increased and decreased on the windward surface, in general. The flow over the aeroshell forebody remained subsonic for the present range of angles-of-attack, and became supersonic only upon the flow expansion around the shoulder. The value of dp/ds increased along most of the symmetry plane with angle-of-attack (especially just downstream of the nose and near the stagnation point), but decreased

just upstream of the nose and along rays approximately 60-deg off of the windward centerline.

The effects of freestream Reynolds number are shown in Figure 7 at $\alpha = 16$ -deg. As the freestream Reynolds number increased, δ and Θ decreased over the entire forebody as expected. M_e stayed approximately constant with increasing freestream Reynolds number. The value of dp/ds decreased over the entire forebody except directly downstream of the nose as Re_∞ increased.

Smooth Model Surface Heating Data

The non-dimensional heating data for the baseline MSL model are shown along the model centerline in Figure 8 and the corresponding images are shown in Figure 9. The data are plotted versus the non-dimensional distance ratio r/R . The heating ratio, h/h_{FR} , near the nose varied from approximately 0.68 at $\alpha = 0$ -deg to approximately 0.72 at $\alpha = 20$ -deg. The heating ratio on the leeward surface of the forebody decreased to values ranging from 0.28 to 0.40 as angle-of-attack decreased from 20-deg to 0-deg and remained at these levels to the shoulder. Heating levels began to rise as the flow reached r/R of approximately 0.9. The rapid expansion of the inviscid flow around the corner forms a large favorable pressure

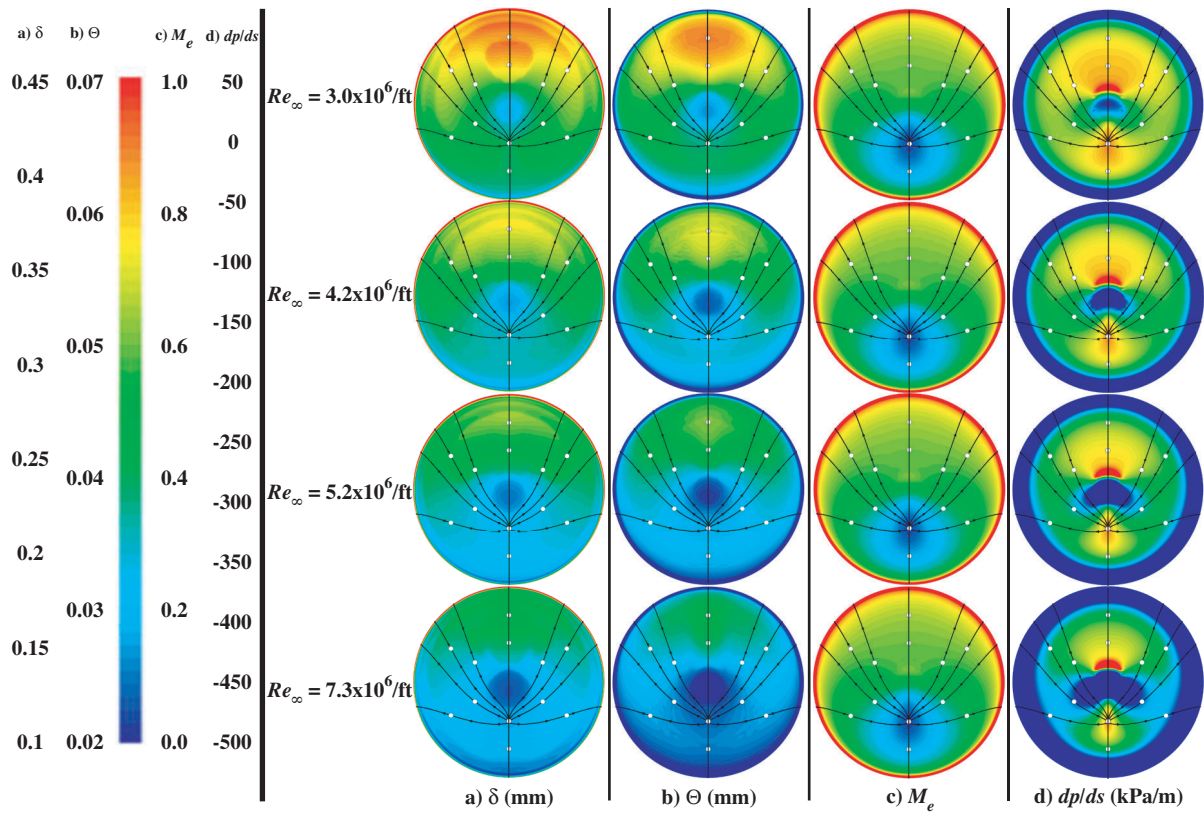


Figure 7: Effect of freestream Reynolds number on boundary layer properties at $\alpha = 16$ -deg.

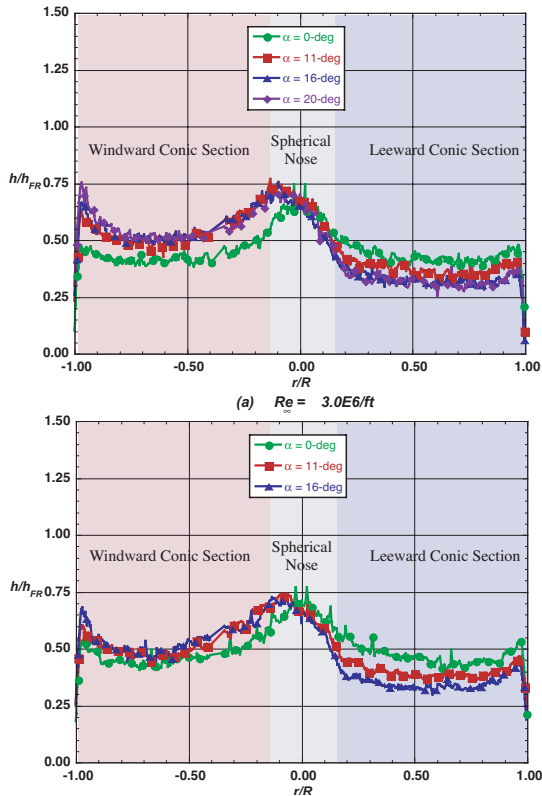


Figure 8: Smooth model centerline heating

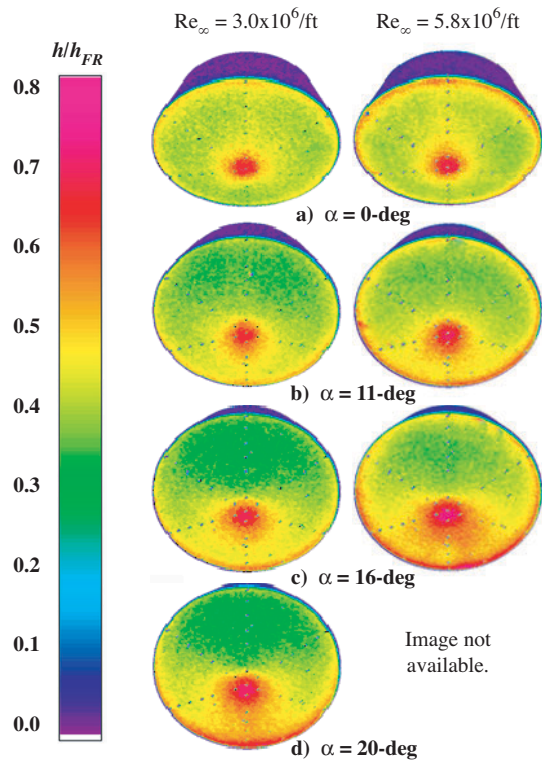


Figure 9: Smooth model images.

gradient, which results in a reduction of the boundary layer thickness¹⁴. This increased heating near the shoulder increased with Reynolds number due to a further decrease in boundary layer height.

The heating ratio on the conical portion of the windward surface decreased from the levels on the nose to approximately $h/h_{FR} = 0.50$ for all non-zero angles-of-attack, then increased to between $h/h_{FR} = 0.46$ for $\alpha = 0$ -deg up to $h/h_{FR} = 0.75$ for $\alpha = 20$ -deg near the shoulder due to expansion of the flow.

Cavity Parametric Model Surface Heating Data

The non-dimensional heating data extracted from the cavity parametric models were plotted beginning at the cavity centers and continuing along the center of the transitional/turbulent wedge which extended downstream from the cavity to the location of maximum diameter (see Fig. 4; when a cavity did not produce a wedge of increased heating, the data were taken along the cut location from a run that did trip the flow). The heating data are plotted versus the non-dimensional distance s/R , which is the distance from the center of the cavity over the surface of the model to the outer diameter of the model non-dimensionalized by the model radius. Included with every cavity plot is a comparison with data extracted along the same line from the baseline smooth model at $Re_\infty = 3.0 \times 10^6$ /ft.

The presence of a cavity may result in high, localized heating at the downstream edge of the cavity due to flow separation and reattachment within the cavity, and may be accompanied by viscous effects downstream of its location (i.e. boundary layer transition). A cavity's ability to influence these parameters will be referred to as its effectiveness.

The effect of cavity diameter at three Reynolds numbers is shown in Fig. 10. As expected, the effectiveness of the cavities is shown to increase as Re_∞ increases. This is because the height of the boundary layer decreased as Re_∞ increased (Fig. 7). Also as expected, the larger the cavity size, the greater the effect on the state of the boundary layer. The effectiveness of the cavities ranged from essentially zero at the lower values of Re_∞ to an increase in downstream heating levels of approximately 325% for $Re_\infty = 7.3 \times 10^6$ /ft (see Ref. 4 for comparison to computed turbulent values).

As angle-of-attack was increased (Fig. 11), the effectiveness of a cavity was strongly influenced by its location on the forebody. Cavities at both radial locations for $\theta = 120$ -deg and 240 -deg became more effective with increasing angle-of-attack; and also at $r/R =$

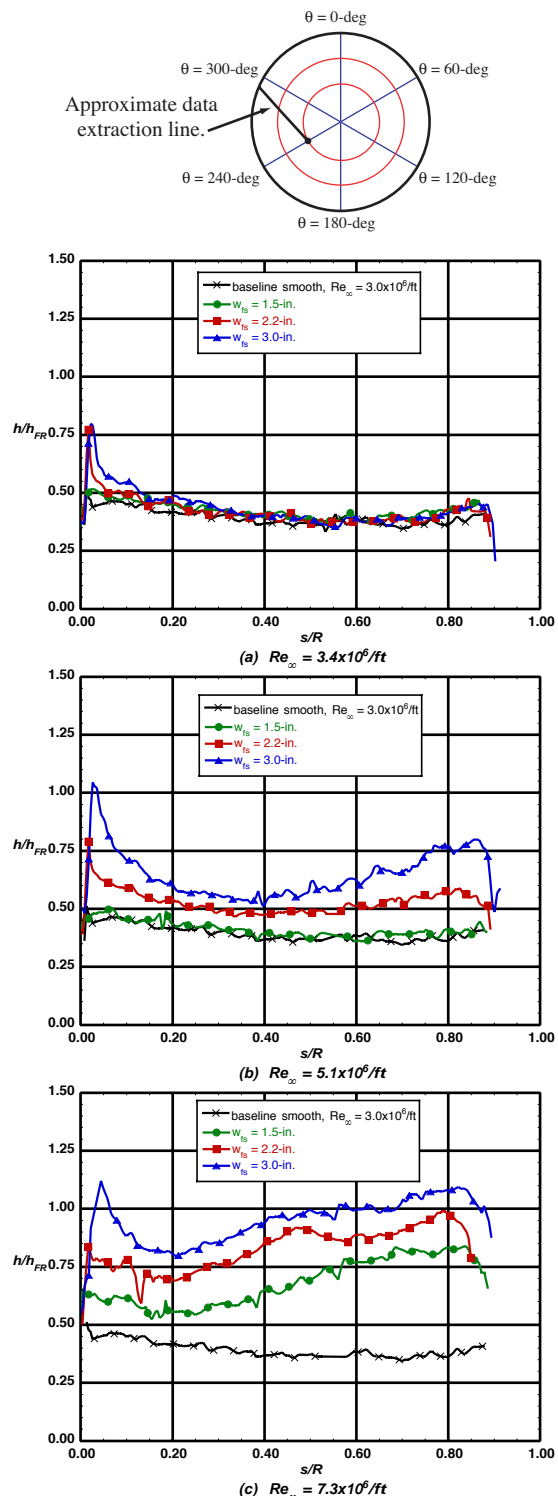


Figure 10: Effect of cavity diameter at $\alpha = 16$ -deg and $\theta = 240$ -deg for $Re_\infty = 3.4 \times 10^6$, 5.1×10^6 , and 7.3×10^6 /ft.

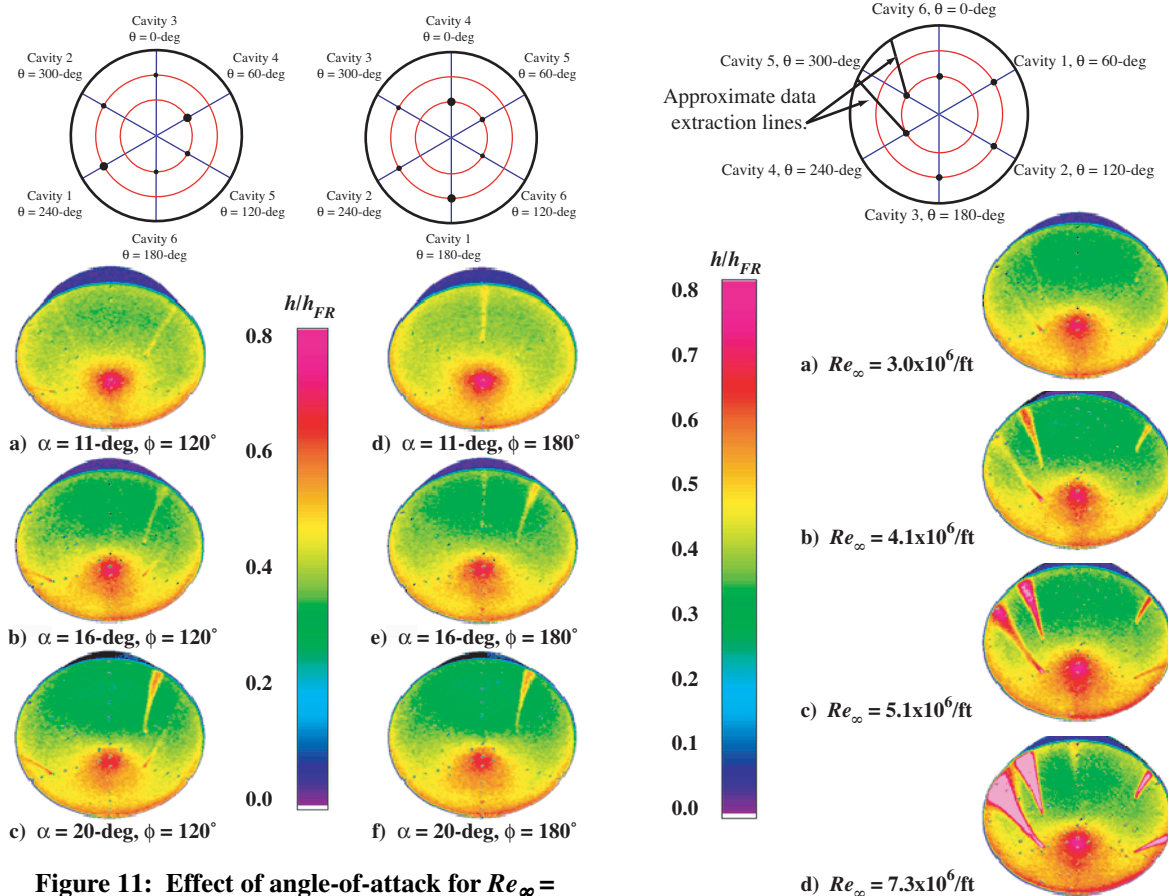


Figure 11: Effect of angle-of-attack for $Re_\infty = 3.4 \times 10^6/\text{ft}$ at $\phi = 180\text{-deg}$.

0.41 for $\theta = 60\text{-deg}$ and 300-deg . These locations correspond to regions at which both δ and Θ either remained constant or decreased slightly as angle-of-attack increased. The cavities that became less effective were located at both radial locations on the leeward centerline and at $r/R = 0.70$ at $\theta = 60\text{-deg}$ and 300-deg . These locations correspond to regions at which δ and Θ were increasing with angle-of-attack. The windward centerline cavities remained essentially ineffective over the angle-of-attack range studied. A local increase in heating levels was observed, but no downstream effect was recorded.

When a cavity caused the boundary layer to become transitional for the non-zero angles-of-attack studied, there were two distinct trends the downstream heating levels followed (Fig. 12). The first trend (Fig. 12.e) was an immediate increase in the heating level, followed by a gradual decrease and then a gradual increase with s/R for higher Reynolds numbers. Cavities exhibiting this behavior were located at both radial positions on the windward surface of the aeroshell forebody, as well as at $r/R = 0.41$ for $\theta = 60\text{-deg}$ and 300-deg at $\alpha = 11\text{-deg}$. These locations correspond to regions where δ and Θ were relatively

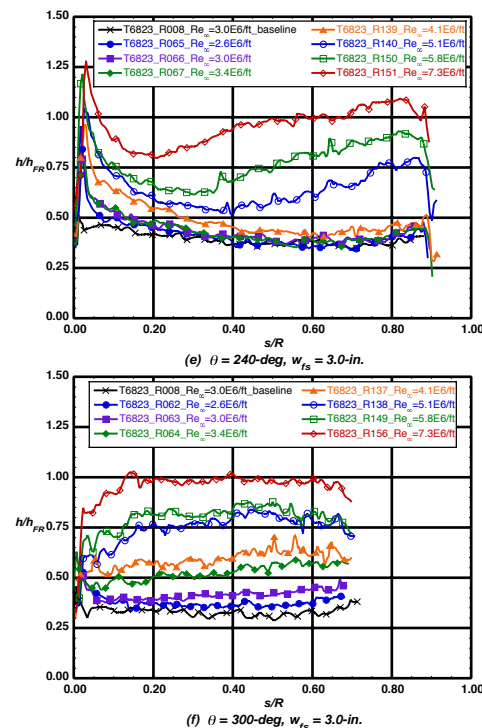


Figure 12: Effect of Re_∞ for $\alpha = 16\text{-deg}$, $\phi = 300\text{-deg}$.

low (compared to the second pattern) and the downstream pressure gradients were strongly negative. The second trend (Fig. 12.f) was an immediate, relatively small increase in heating downstream of the cavity followed by a gradual increase in heating levels. Cavities exhibiting this behavior were located at both radial locations on the leeward centerline and at $r/R = 0.70$ at $\theta = 60$ -deg and 300 -deg at all angles-of-attack. The $r/R = 0.41$, $\theta = 60$ -deg and 300 -deg locations were included in this pattern at $\alpha = 11$ -deg. These locations correspond to regions where δ and Θ were relatively large (compared to the first pattern) and the downstream pressure gradients were greater than those of the first pattern.

The present measurements in the 20-Inch Mach 6 Air Tunnel for the proposed MSL aeroshell demonstrated that the effectiveness of a given cavity depends on the local values of δ and Θ . As these parameters decreased, the effectiveness of the cavity was shown to increase. One method of predicting boundary layer transition due to the presence of a cavity is to compare the Reynolds number based on momentum thickness with the ratio of cavity diameter to boundary layer height (w/δ). One can expect the effectiveness of a constant cavity size to increase with w/δ , as shown. This correlation is discussed in Ref. 4 for the proposed MSL aeroshell.

CONCLUSIONS

An experimental aeroheating study was conducted on a proposed Mars Smart Lander aeroshell in the NASA Langley 20-Inch Mach 6 Air Tunnel using the technique of phosphor thermography. This test was conducted in order to determine if heat shield cavities of significant size have an impact on forebody heating. The study concluded that forebody cavities did indeed have a profound impact on heating levels and should be considered in the design process of the Mars Smart Lander.

This study was complemented by an analysis of boundary layer quantities obtained from thin-layer, laminar, Navier-Stokes flowfield solutions. The computational results quantified the boundary layer height and momentum thickness as functions of freestream Reynolds number, angle-of-attack, and location on the aeroshell forebody. Tests were conducted on baseline smooth and cavity parametric Mars Smart Lander aeroshell models at freestream Reynolds numbers from $2.6 \times 10^6/\text{ft}$ to $7.3 \times 10^6/\text{ft}$.

Smooth model heating data showed that heating levels near the shoulder increased due to the thinning

of the boundary layer. This increase in heating near the shoulder increased with Reynolds number.

Cavity parametric model heating data showed that the effectiveness of a cavity depended on the cavity diameter and boundary layer height. As the cavity diameter increased, the effectiveness of the cavity increased. As boundary layer height decreased, the effectiveness of a cavity increased. The presence of a cavity was shown to cause the increase in downstream heating levels by as much as 325% due to boundary layer transition.

The present study has provided a comprehensive data base (approximately 800 data points) on the state of the boundary layer of a proposed MSL aeroshell with cavities located on the forebody heat shield. This database was used to formulate a transition correlation to predict the onset of boundary layer transition in a companion paper by Hollis⁴.

ACKNOWLEDGEMENTS

The authors would like to acknowledge the contributions of the following individuals to this research: Jonny Ellis, Grace Gleason, and Roland Hatten for operation of the 20-Inch Mach 6 Air Tunnel and data acquisition support; Joe Powers and Mark Griffith for fabrication of the ceramic models; Karl Edquist and Mary Kae Lockwood for programmatic support; and Mark McMillin for providing the CAD files necessary to fabricate the models.

REFERENCES

- ¹Lockwood, M.K., Powell, R.W., Graves, C.A., Carman, G.L., "Entry System Design Considerations for Mars Landers," American Astronautical Society Paper 01-023, January/February 2001.
- ²Cheatwood, F.M., Merski, N.R., Riley, C.J., Mitcheltree, R.A., "Aerothermodynamic Environment Definition for the Genesis Sample Return Capsule," AIAA Paper 2001-2889, June 2001.
- ³Edquist, K. and Loomis, M., "Aeroheating Environments for Mars Smart Lander Configurations," AIAA Paper 2002-4505, August 2002.
- ⁴Hollis, B.R., Liechty, D.S., "Boundary Layer Transition Correlations and Aeroheating Predictions for Mars Smart Lander," AIAA Paper 2002-2745, June 2002.
- ⁵Gnoffo, P.A., "An Upwind-Biased, Point-Implicit Algorithm for Viscous, Compressible Perfect-Gas Flows," NASA TP-2953, February 1990.

⁶Cheatwood, F.M., Gnoffo, P.A., “User’s Manual for the Langley Aerothermodynamic Upwind Relaxation Algorithm (LAURA),” NASA TM-4674, April 1996.

⁷Micol, J.R., “Hypersonic Aerodynamic/Aerothermodynamic Testing Capabilities at Langley Research Center: Aerothermodynamic Facilities Complex,” AIAA Paper 95-2107, June 1995.

⁸Buck, G.M., “Automated Thermal Mapping Techniques Using Chromatic Image Analysis,” NASA TM 101554, April 1989.

⁹Buck, G.M., “Surface Temperature/Heat Transfer Measurement Using a Quantitative Phosphor Thermography System,” AIAA Paper 91-0064, January 1991.

¹⁰Merski, N.R., “A Relative-Intensity, Two-Color Phosphor Thermography System,” NASA TM 104123, September 1991.

¹¹Merski, N.R., “Reduction and Analysis of Phosphor Thermography Data with the IHEAT Software Package,” AIAA Paper 98-0712, January 1998.

¹²Buck, G.M., and Vasques, P., “An Investment Ceramic Slip-Casting Technique for Net-Form, Precision, Detailed Casting of Ceramic Models,” U.S. Patent 5,266,252, November 1993.

¹³Fay, J.A., and Riddell, F.R., “Theory of Stagnation Point Heat Transfer in Dissociated Air,” *Journal of Aeronautical Sciences*, Vol 25, No. 2, 1958, pp. 73-85.

¹⁴Anderson, J.D., Jr.: *Hypersonic and High Temperature Gas Dynamics*, McGraw-Hill Book Co., New York, 1989, pp. 265-266.

Re_∞ (1/ft)	M_∞	T_∞ (K)	ρ_∞ (kg/m ³)	U_∞ (m/s)	Re_∞ (1/m)	h_{FR} (kg/m ² -s)	q_{FR} (W/cm ²)
2.1x10⁶	5.95	62.0	3.35x10 ⁻²	938x6	7.07x10 ⁶	0.283	5.70
2.6x10⁶	5.97	62.2	4.05x10 ⁻²	943.0	8.55x10 ⁶	0.313	6.45
3.0x10⁶	5.98	62.2	4.62x10 ⁻²	944.4	9.79x10 ⁶	0.335	6.95
3.4x10⁶	5.99	61.6	5.29x10 ⁻²	940.1	1.13x10 ⁷	0.356	7.25
4.2x10⁶	6.00	61.3	6.41x10 ⁻²	940.4	1.37x10 ⁷	0.392	7.95
4.6x10⁶	6.01	63.5	7.25x10 ⁻²	958.5	1.52x10 ⁷	0.427	9.48
5.1x10⁶	6.02	63.4	7.92x10 ⁻²	958.7	1.67x10 ⁷	0.446	9.92
5.8x10⁶	6.03	62.8	8.99x10 ⁻²	955.6	1.91x10 ⁷	0.474	10.4
7.3x10⁶	6.06	62.3	1.13x10 ⁻¹	954.6	2.41x10 ⁷	0.529	11.5

Table 3: Nominal flow conditions of the Langley 20-Inch Mach 6 Air Tunnel.